

## Spin-dependent cross sections from the three-body photodisintegration of $^3\text{He}$ at incident energies of 12.8 and 14.7 MeV

G. Laskaris,<sup>1,2,\*</sup> Q. Ye,<sup>1,2,†</sup> B. Lalremruata,<sup>1,2,‡</sup> Q. J. Ye,<sup>1,2</sup> M. W. Ahmed,<sup>1,2,3</sup> T. Averett,<sup>4</sup> A. Deltuva,<sup>5</sup> D. Dutta,<sup>6</sup> A. C. Fonseca,<sup>5</sup> H. Gao,<sup>1,2</sup> J. Golak,<sup>7</sup> M. Huang,<sup>1,2</sup> H. J. Karwowski,<sup>1,8</sup> J. M. Mueller,<sup>1,2</sup> L. S. Myers,<sup>1,2,§</sup> C. Peng,<sup>1,2</sup> B. A. Perdue,<sup>1,2,||</sup> X. Qian,<sup>1,2,¶</sup> P. U. Sauer,<sup>9</sup> R. Skibiński,<sup>7</sup> S. Stave,<sup>1,2,#</sup> J. R. Tompkins,<sup>1,8,\*\*</sup> H. R. Weller,<sup>1,2</sup> H. Witała,<sup>7</sup> Y. K. Wu,<sup>1,2</sup> Y. Zhang,<sup>1,2</sup> and W. Zheng<sup>1,2</sup>

<sup>1</sup>Triangle Universities Nuclear Laboratory, Durham, North Carolina 27708, USA

<sup>2</sup>Department of Physics, Duke University, Durham, North Carolina 27708, USA

<sup>3</sup>Department of Mathematics and Physics, North Carolina Central University, Durham, North Carolina 27707, USA

<sup>4</sup>College of William and Mary, Williamsburg, Virginia 23187, USA

<sup>5</sup>Centro de Física Nuclear da Universidade de Lisboa, P-1649-003 Lisboa, Portugal

<sup>6</sup>Mississippi State University, Starkville, Mississippi 39762, USA

<sup>7</sup>Marian Smoluchowski Institute of Physics, Jagiellonian University, PL-30059 Kraków, Poland

<sup>8</sup>Department of Physics and Astronomy, University of North Carolina at Chapel Hill, Chapel Hill, North Carolina 27599, USA

<sup>9</sup>Institut für Theoretische Physik, Leibniz Universität Hannover, D-30167 Hannover, Germany

(Received 21 October 2013; revised manuscript received 16 January 2014; published 11 February 2014)

The first measurement of the three-body photodisintegration of polarized  $^3\text{He}$  using a circularly polarized photon beam has been performed at incident energies of 12.8 and 14.7 MeV. This measurement was carried out at the high-intensity  $\gamma$ -ray source located at Triangle Universities Nuclear Laboratory. A high-pressure  $^3\text{He}$  target, polarized via spin exchange optical pumping with alkali metals, was used in the experiment. The spin-dependent double- and single-differential cross sections from  $^3\text{He}(\gamma, n)pp$  for laboratory angles varying from  $30^\circ$  to  $165^\circ$  are presented and compared with state-of-the-art three-body calculations. The data reveal the importance of including the Coulomb interaction between protons in the three-body calculations.

DOI: [10.1103/PhysRevC.89.024002](https://doi.org/10.1103/PhysRevC.89.024002)

PACS number(s): 25.20.-x, 29.25.Pj, 67.30.ep

### I. INTRODUCTION

$^3\text{He}$  has been used as an effective target to study the neutron. Polarized  $^3\text{He}$  is particularly important as an effective polarized neutron target because in the ground state the two protons are predominantly in an  $S$  state in which their spins cancel and the nuclear spin is carried by the unpaired neutron. Recent experimental advances such as the availability of polarized beams and hyperpolarized  $^3\text{He}$  targets have allowed for the extraction of spin-dependent neutron structure properties such as the electromagnetic form factors [1–7] and the spin structure functions [8–12]. Hyperpolarized  $^3\text{He}$  targets have also been used in the search for a new spin-dependent force between polarized neutrons and unpolarized nucleons [13]. An important uncertainty in extracting the neutron information from  $^3\text{He}$  is due to the nuclear corrections, which can only be improved by testing theoretical calculations of three-body systems by experiments such as polarized photodisintegration of  $^3\text{He}$ .

State-of-the-art calculations for the three-body breakup of  $^3\text{He}$  have been performed using the Faddeev [14] and

Alt, Grassberger, and Sandhas (AGS) [15] equations. The calculations by Deltuva *et al.* [16] are based on the AGS equations and employ the coupled-channel extension of the charge-dependent Bonn (CD Bonn) nucleon-nucleon ( $NN$ ) potential [17–19], including explicit excitation of a nucleon into a  $\Delta$ -isobar, called CD Bonn +  $\Delta$ -isobar [20]. In the three-nucleon ( $3N$ ) system the  $\Delta$ -isobar excitation yields effective  $3N$  force and effective two-nucleon and  $3N$  currents that are mutually consistent [16]. In addition to single-baryon and meson exchange electromagnetic currents, the relativistic single-nucleon charge corrections (RC) are taken into account [16]. The proton-proton Coulomb interaction is also included using the method of screening and renormalization [21]. The calculations by Skibiński *et al.* solve the Faddeev equations by using the Argonne V18 (AV18)  $NN$  potential [22] and the Urbana IX (UIX)  $3N$  force [23], taking into account the single-nucleon currents and the two most important meson exchange currents, namely the seagull and pion-in-flight terms [24].

In addition, Rozpędzik and collaborators [25] have carried out calculations of the three-body photodisintegration of  $^3\text{He}$  using chiral effective field theory [26] ( $\chi$ EFT) in the Faddeev framework including the well-known one-pion exchange contributions and the long-range two-pion exchange parts of meson exchange currents at next-to-leading-order derived with the method of unitary transformation [27]. The results are compared with the calculations obtained with the AV18  $NN$  potential and the related exchange currents, and good agreement is found between the two theories [25]. However, the uncertainties of  $\chi$ EFT are much larger compared

\*georgios.laskaris@duke.edu

†Present address: UMD, College Park, MD 20742, USA.

‡Present address: Mizoram University, Aizawl 796004, India.

§Present address: TJNAF, Newport News, VA 23606, USA.

||Present address: LANL, Los Alamos, NM 87544, USA.

¶Present address: BNL, Upton, NY 11973, USA.

#Present address: PNNL, Richland, WA 99352, USA.

\*\*Present address: MSU, East Lansing, MI 48824, USA.

to the uncertainties of the calculations based on AV18 and neither approach includes the Coulomb force between the two protons in  $3N$  scattering states of  ${}^3\text{He}$ . These uncertainties vote for inclusion of nuclear forces and currents in higher orders of chiral expansion to describe the  ${}^3\text{He}$  photodisintegration. Unfortunately, such calculations are not available; thus we compare the results of this work only with the calculations obtained based on the computational approach of Refs. [16,24].

The experiment on the three-body photodisintegration of  ${}^3\text{He}$  is of further importance for the investigation of the Gerasimov-Drell-Hearn (GDH) sum rule [28]. The GDH sum rule relates the energy-weighted difference of the helicity-dependent total photoabsorption cross sections for target spin and photon helicity parallel and antiparallel to the anomalous magnetic moment of the target (nuclei or nucleons). There have been significant efforts to test the GDH sum rule on the proton [29], neutron [30], and deuteron [31,32]. For the case of  ${}^3\text{He}$ , the relevant energy range is from the two-body breakup threshold ( $\sim 5.5$  MeV) up to  $\sim 40$  MeV. According to the theoretical calculations [16,24], this energy region dominates the integrand of  ${}^3\text{He}$  below the pion production threshold [33]. The calculations also show that the contribution from the three-body breakup channel to the GDH integral is larger than that from the two-body breakup. Therefore, the measurements of the spin-dependent cross sections of  ${}^3\text{He}(\vec{\gamma}, n)pp$  not only test the dynamics underlying the modern three-body calculations but also represent an important step towards the investigation of the GDH sum rule when one combines the measurements above the pion production threshold from other laboratories [11,34] with our reported measurements below it [35] and upcoming measurements of the two-body breakup channel.

## II. THE EXPERIMENT

We report the first measurements of three-body photodisintegration of  ${}^3\text{He}$  using a longitudinally polarized  ${}^3\text{He}$  target and a circularly polarized  $\gamma$ -ray beam. Beam energies of 12.8 and 14.7 MeV were used. The experiment was carried out at the high-intensity  $\gamma$ -ray source (HI $\gamma$ S) at Triangle Universities Nuclear Laboratory. The facility provided nearly monoenergetic,  $\sim 100\%$  circularly polarized  $\gamma$ -ray beams [36]. The photon beam was collimated using a 12-mm-diameter collimator resulting in beam energy spreads ( $\Delta E_\gamma/E_\gamma$ ) of  $\sim 3\%$  at 12.8 MeV and  $\sim 5\%$  at 14.7 MeV. A high-pressure  ${}^3\text{He}$  cell was employed as a target and the neutrons from the three-body breakup of  ${}^3\text{He}$  were detected using 16 liquid scintillator detectors. The photon flux was monitored with a  $\text{D}_2\text{O}$  target and two additional liquid scintillator detectors. A schematic view of the experimental apparatus including the  ${}^3\text{He}$  target system and optics support, the detectors, and the  $\text{D}_2\text{O}$  flux monitor is shown in Fig. 1.

The  ${}^3\text{He}$  target cell was a one-piece glassware made of Pyrex glass consisting of two chambers: a spherical pumping chamber 8.1 cm in diameter and a 39.3-cm-long and 2.9-cm-diameter cylindrical target chamber having entrance and exit windows 250  $\mu\text{m}$  thick. The two chambers were connected through a 9.1-cm-long transfer tube which was 7.8 mm in diameter. All length measurements refer to the

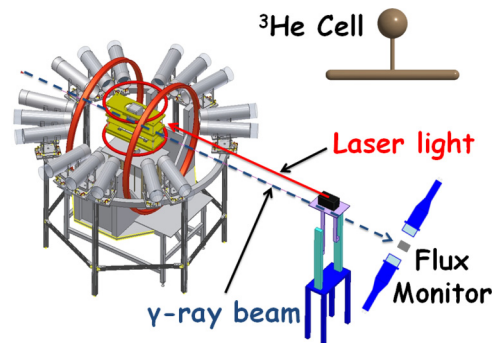


FIG. 1. (Color online) Schematic of the experimental apparatus. The movable target system (yellow [light gray]) that was used to cycle between the  ${}^3\text{He}$  target and the  $\text{N}_2$  reference cell is surrounded by 16 liquid scintillator detectors placed inside  $\mu$ -metal tubes (gray). The Helmholtz coils (red [dark gray]) provided the holding field. The movable support of the optics that was employed to polarize the  ${}^3\text{He}$  target and the  $\text{D}_2\text{O}$  flux monitor can be seen in the bottom right corner of the figure, next to the flux monitor.

inner dimensions of the target cell. A mixture of Rb and K alkali-metals was inside the pumping chamber of the  ${}^3\text{He}$  target cell. A circularly polarized light provided by one  $\sim 60$ -W Coherent DUO-FAP broadband and three VBG-locked Comet  $\sim 30$ -W narrowband diode lasers was incident on the pumping chamber. The pumping chamber was heated up to  $\sim 473$  K. To circularly polarize the laser light, a set of optics was used positioned downstream from the  ${}^3\text{He}$  target. The Rb atoms were optically pumped and polarized, and they in turn transferred their polarization to K atoms. Spin exchange collisions between Rb, K, and  ${}^3\text{He}$  atoms transferred the polarization to  ${}^3\text{He}$  nuclei through hyperfine interactions [37]. The filling density of  ${}^3\text{He}$  was  $6.48 \pm 0.1$  amg.<sup>1</sup> In addition to the  ${}^3\text{He}$  gas, about 0.1 amg of  $\text{N}_2$  gas was in the target as a buffer gas.

A 20.2-G magnetic holding field was provided to define the  ${}^3\text{He}$  spin direction by a pair of Helmholtz coils  $\sim 170$  cm in diameter. The nuclear magnetic resonance–adiabatic fast passage technique [38] (NMR-AFP) was employed to measure the polarization of  ${}^3\text{He}$  target. This technique was calibrated daily using electron paramagnetic resonance (EPR) [39]. The polarization using the EPR measurement can be determined as in Ref. [40]:

$$P_{pc} = \frac{2\Delta\nu_{\text{EPR}}}{2 \times \frac{2\mu_0}{3} \frac{d\nu_{\text{EPR}}}{dB} \kappa \mu_{{}^3\text{He}} n_{pc}} \quad (1)$$

where  $P_{pc}$  is the polarization of the pumping chamber,  $\Delta\nu_{\text{EPR}}$  is the EPR frequency shift in kHz,  $\frac{d\nu_{\text{EPR}}}{dB} = 0.47 + 7.38 \times 10^{-4} B$  (MHz) [41] with  $B$  being the holding field magnitude,  $\mu_0$  is the permeability of vacuum,  $\mu_{{}^3\text{He}}$  is the magnetic moment of  ${}^3\text{He}$ , and  $n_{pc}$  is the number density of  ${}^3\text{He}$  in the pumping chamber. The constant  $\kappa = 4.52 + 0.00934T_{pc}$  [39], where  $T_{pc}$  is the pumping chamber temperature.  $\kappa$  is related to

<sup>1</sup>An amagat is the number density of an ideal gas at  $0^\circ\text{C}$  and 1 atmosphere: 1 amg =  $2.6894 \times 10^{19}$  atoms/cm<sup>3</sup>.

the spin-exchange cross section and is independent of  $^3\text{He}$  polarization.  $P_{tc}$ , the polarization of the target chamber, is given by [42]  $P_{tc} = P_{pc} \times \frac{d_{tc}}{d_{tc} + \Gamma_{tc}}$ , where  $d_{tc}$  is the diffusion rate from the target chamber to the pumping chamber and  $\Gamma_{tc}$  is the relaxation rate of  $^3\text{He}$  in the target chamber. Both diffusion and relaxation rates were measured to be  $\sim 1/50$  min and  $\sim 1/50$  h, respectively.  $P_{tc}$  was found to be  $\sim 1.5\%$  (relative) less than  $P_{pc}$ , and varied between 38% and 43%. A more detailed description of the polarized  $^3\text{He}$  target can be found in Refs. [40,42]. The NMR-AFP, employed to measure the polarization of  $^3\text{He}$  target during the experiment, normally resulted in a minor depolarization of the cell on the order of absolute 1%. Since the cell was constantly polarized, the polarization could recover after  $\sim 1$  h. The polarization of the target was flipped every 15 min, which was found to be sufficient to reduce systematic uncertainties due to target polarization drift to a negligible level. The helicity of the beam was flipped only once towards the end of the experiment because it took a significant amount of time.

A reference cell identical to the target chamber of the  $^3\text{He}$  cell and filled with only 0.1 amg of  $\text{N}_2$  gas was employed for measuring the backgrounds. Although Rb and K can leak into the transfer tube and the target chamber during spin exchange optical pumping [37], they immediately condense on the cell walls due to the temperature gradient. The temperature of the target chamber was measured during the experiment and did not exceed  $\sim 300$  K. The alkali-metal number densities in the target chamber can be calculated based on the vapor pressure curves given in Ref. [43] and were found to be  $\sim 10^{10}$  and  $10^9$   $\text{cm}^{-3}$  for Rb and K, respectively. Given the very low alkali-metal number densities, the measured photo-neutron cross sections of Rb [44,45], and K [46,47], and the integrated photon flux during the experiment, the neutron background from the alkali-metals in the target chamber was found to be negligible.

To reduce systematic uncertainties, the  $^3\text{He}$  target and the  $\text{N}_2$  reference cell were switched frequently with the help of an integrated stepper motor connected with a jack placed under the  $^3\text{He}$  target apparatus. Another stepper motor was used to move the set of optics vertically following the  $^3\text{He}$  target movement. In this way, the  $^3\text{He}$  target was polarized continuously throughout the experiment.

The neutrons from the three-body photodisintegration of  $^3\text{He}$  were detected using 16 liquid scintillator detectors. Each of the neutron detectors consists of a cylindrical cell 12.7 cm in diameter and 5.1 cm long filled with BC-501A [48] organic scintillating liquid coupled to a photomultiplier tube. The detectors were placed 1 m away from the center of the target at laboratory angles  $30^\circ$ ,  $45^\circ$ ,  $75^\circ$ ,  $90^\circ$ ,  $105^\circ$ ,  $135^\circ$ ,  $150^\circ$ , and  $165^\circ$ . The photomultiplier tubes were inside  $\mu$ -metal shields to protect the photomultiplier tubes from the magnetic field of the Helmholtz coils.

A cylindrical  $\text{D}_2\text{O}$  cell, 4.74 cm long and 4.08 cm in diameter, along with two neutron detectors was employed as a  $\gamma$ -ray flux monitor. The setup was positioned downstream of the target and the detectors were placed at  $90^\circ$  on either side and 50 cm away of the  $\text{D}_2\text{O}$  target. The detectors counted neutrons from the  $^2\text{H}(\gamma, n)p$  reaction. The integrated photon flux,  $N_\gamma$ ,

was calculated based on the well-known total cross sections [49,50] and angular distributions [51] of the neutrons produced by deuteron photodisintegration. A detailed description of the extraction of the photon flux using the  $\text{D}_2\text{O}$  monitor can be found in Refs. [52,53]. The photon intensity throughout the experiment was  $\sim 1-2 \times 10^8 \gamma/s$ .

### III. DATA ANALYSIS

The pulse height (PH), the time-of-flight (TOF), and the pulse shape discrimination (PSD) parameter between photons and neutrons were recorded for each event in terms of analog-to-digital converter (ADC), time-to-digital converter (TDC), and PSD channels. The calibration of the ADC channels to PH was performed using a  $^{137}\text{Cs}$  source, which emits a single  $\gamma$ -ray at the energy of 662 keV. Source runs were taken several times per day to ensure the stability of the detectors. The location of the  $^{137}\text{Cs}$  Compton edge together with the ADC pedestal (the channel readout when no signal is present) were used to convert the ADC channels to PH. A detailed description of the PH calibration can be found in Refs. [52,53]. The PH thresholds for the primary detectors and the detectors used as the  $\text{D}_2\text{O}$  flux monitor were  $\frac{5}{16} \times$  and  $1 \times$  the cesium edge location, respectively. The efficiency changes rapidly as a function of neutron energy below 1.5 MeV and varies from  $\sim 36\%$  at  $\sim 2$  MeV to  $\sim 31\%$  at the maximum expected neutron energy of  $\sim 5$  MeV. Since the efficiency changes rapidly below 1.5 MeV, we report cross sections only for neutrons above this energy.

TOF is defined as the time that it takes a neutron to travel from the center of the target to the detector. The TDC calibration was performed using two additional targets. The targets were an aluminum rod 12.7 mm in diameter positioned with its axis vertically with respect to the beam and a  $\text{D}_2\text{O}$  target  $50.3 \pm 0.9$  mm in length and  $31.8 \pm 0.1$  mm in diameter placed at the center of the detector array. Spectra were obtained from the detection of  $\gamma$  rays scattered from the aluminum rod. The centroid-timing value of these  $\gamma$  rays,  $\text{TDC}_\gamma$ , was the zero point of the TDC calibration. The formula used for the TOF calibration was  $\text{TOF} = \text{TDC}_{\text{cal}} \times (\text{TDC} - \text{TDC}_\gamma) + d/c$ , where  $\text{TDC}_{\text{cal}}$  is the conversion factor of the TDC channels to nanoseconds,  $d$  is the distance from the center of the target to the detector, and  $c$  is the speed of light. The addition of the  $d/c$  factor was necessary in order to account for the fact that it takes  $d/c$  ns for a  $\gamma$  ray to travel from the center of the target to the detector. To find the  $\text{TDC}_{\text{cal}}$  factor, the TDC neutron spectra acquired from the  $\text{D}_2\text{O}$  target were used together with the results of a  $d(\gamma, n)p$  GEANT4 simulation. The  $\text{TDC}_{\text{cal}}$  factor was given by  $(\text{TOF}_n - \text{TOF}_\gamma)/(\text{TDC}_n - \text{TDC}_\gamma)$  where  $\text{TDC}_n$  is the centroid value of the neutron peak at the TDC spectra and  $\text{TOF}_n$  ( $\text{TOF}_\gamma$ ) is the simulated TOF that it takes for a neutron ( $\gamma$  ray) to reach the detector. The  $\text{TDC}_{\text{cal}}$  was calculated for each detector, individually. Once the  $\text{TDC}_{\text{cal}}$  was found for one incident photon energy, no further tuning was required for the other incident energy. The extracted TOF for each event was used to reconstruct the outgoing neutron energy,  $E_n(\text{TOF}) = m_n / \sqrt{1 - (\frac{d}{\text{TOF} \times c})^2} - m_n$  with  $m_n$  being the neutron mass, assuming the neutrons originate from the center of the target.

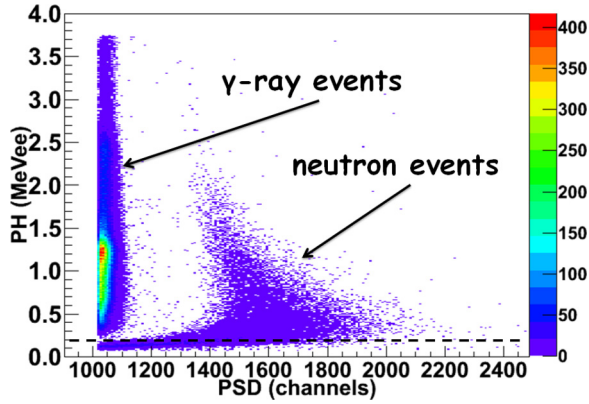


FIG. 2. (Color online) A PSD vs PH spectrum for a detector placed at  $90^\circ$ . The data were acquired at  $E_\gamma = 14.7$  MeV. The neutron events are well separated from the  $\gamma$ -ray events. The PH cut location is indicated by the long-dashed line.

Apart from the neutrons, the liquid scintillator detectors are capable of detecting  $\gamma$  rays. The detector signals (neutrons or photons) were processed through the commercially available MPD-4 modules manufactured by Mesytec [54]. Each MPD-4 module generates an adjustable PSD parameter which can discriminate neutrons from photons. Larger PSD values correspond to neutrons while smaller values are from  $\gamma$  rays. The PSD spectra remained uncalibrated and different PSD thresholds were applied to each detector.

To identify the neutrons events and discard the  $\gamma$ -ray events, we utilized the correlations between the PH, PSD, and TOF parameters. Initially, a TOF cut at 20 ns was applied to the data in order to reject the  $\gamma$  ray events that arrived at  $\sim 3.3$  ns ( $= d/c$ ). After that, the correlation between the PSD and PH was utilized. Figure 2 shows the two-dimensional histogram of PSD plotted versus PH for events that were collected at the incident photon energy of 14.7 MeV. A hardware threshold was applied at the PSD around channel 1000 to eliminate most of the incident  $\gamma$  rays. The neutron events are located at the right of the histogram and they can be very well separated from the  $\gamma$  rays located at the left of the histogram. The long-dashed line indicates the PH cut location. All the events identified as neutrons and located above the PH cut were kept.

The detected neutron events originated from the reaction under study ( ${}^3\text{He}(\vec{\gamma}, n)pp$ ) and from other ( $\gamma, n$ ) reactions with various elements contained in the Pyrex glass, the air, and the  $\text{N}_2$  inside the  ${}^3\text{He}$  target. The Pyrex glass is composed of elements (as percentage of weight) such as oxygen (54%), silicon (37.7%), boron (4.0%), sodium (2.8%), and aluminum (1.1%). Other elements may also be contained with smaller than 1% contributions to the total composition. O and Si, which are the main components of Pyrex glass, do not undergo ( $\gamma, n$ ) reaction at the energies of our present experiment. B, Al, Na, and N inside the  ${}^3\text{He}$  target cell and in the air undergo ( $\gamma, n$ ) reaction with cross sections, which are in general lower at 12.8 MeV and higher at 14.7 MeV. In order to measure and subtract the overall background neutron yield, a  $\text{N}_2$ -only reference cell was employed. The cuts applied to the  $\text{N}_2$

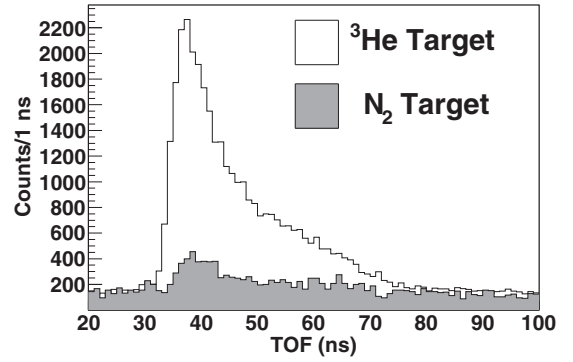


FIG. 3. The TOF spectra of  ${}^3\text{He}$  target in comparison to the  $\text{N}_2$  reference cell target normalized to the same flux for a detector placed at  $90^\circ$ . The data were acquired at  $E_\gamma = 14.7$  MeV.

reference cell data were the same as in the  ${}^3\text{He}$  target case. Figure 3 shows the neutron counts acquired from the  ${}^3\text{He}$  target cell compared to the  $\text{N}_2$ -only reference cell normalized to the same number of photons for a detector placed at a laboratory angle of  $90^\circ$  at an  $\gamma$ -ray beam energy of 14.7 MeV.

The neutrons from the three-body breakup of  ${}^3\text{He}$  detected at  $90^\circ$  are expected to have a maximum energy of  $\sim 4.7$  MeV. This energy corresponds to a TOF of  $\sim 33$  ns as can be seen in Fig. 3. The long tail of the  ${}^3\text{He}$  target TOF spectrum, which extends up to 80 ns, corresponds to neutrons with lower energies. Neutrons with TOF higher than  $\sim 68$  ns (or equivalently with  $E_n$  lower than  $\sim 1.5$  MeV) were not included in the analysis.

#### IV. RESULTS AND DISCUSSION

Neutron energy spectra for the  ${}^3\text{He}$  and  $\text{N}_2$  targets were generated based on the extracted TOF for each incident photon energy and detector angle. The energy spectra of the  ${}^3\text{He}$  and  $\text{N}_2$  targets were normalized to their corresponding integrated photon flux and the neutron background subtracted yield ( ${}^3\text{He}$  neutron events/ $N_\gamma$ ) of  ${}^3\text{He}$  at the  $i$ th energy bin was calculated as  $Y_i^{P/A} = Y_i^{P/A, {}^3\text{He}} - Y_i^{\text{N}_2}$ , where  $Y_i^{P/A, {}^3\text{He}}$  and  $Y_i^{\text{N}_2}$  are the measured yields of  ${}^3\text{He}$  and  $\text{N}_2$  cells. The background subtracted yields were combined and the yields for parallel and antiparallel spin-helicity states were extracted as  $Y_{i,\text{ext}}^{P/A} = \frac{1}{2}[Y_i^P(1 \pm \frac{1}{P_t P_b}) + Y_i^A(1 \mp \frac{1}{P_t P_b})]$ , where  $P_t$  and  $P_b$  are the target and the beam polarization, respectively. The double-differential cross section was defined as

$$\frac{d^3\sigma^{P/A}}{d\Omega dE_n} = \frac{Y_{i,\text{ext}}^{P/A}}{\varepsilon_i^{\text{synt}} \Delta\Omega \Delta E N_t} \quad (2)$$

where  $\varepsilon_i^{\text{synt}}$  is the system efficiency accounting for both the intrinsic efficiency of the neutron detector and the neutron multiple scattering effect calculated at the  $i$ th energy bin,  $\Delta\Omega$  is the acceptance from the 40-cm-long target to the neutron detector,  $\Delta E$  is the width of the neutron energy bin, and  $N_t$  is the  ${}^3\text{He}$  target thickness determined to be  $(8.4 \pm 0.1) \times 10^{21}$  atoms/cm<sup>2</sup>. The system efficiencies  $\varepsilon_i^{\text{synt}}$  were calculated as a function of  $E_n$  using a GEANT4 simulation

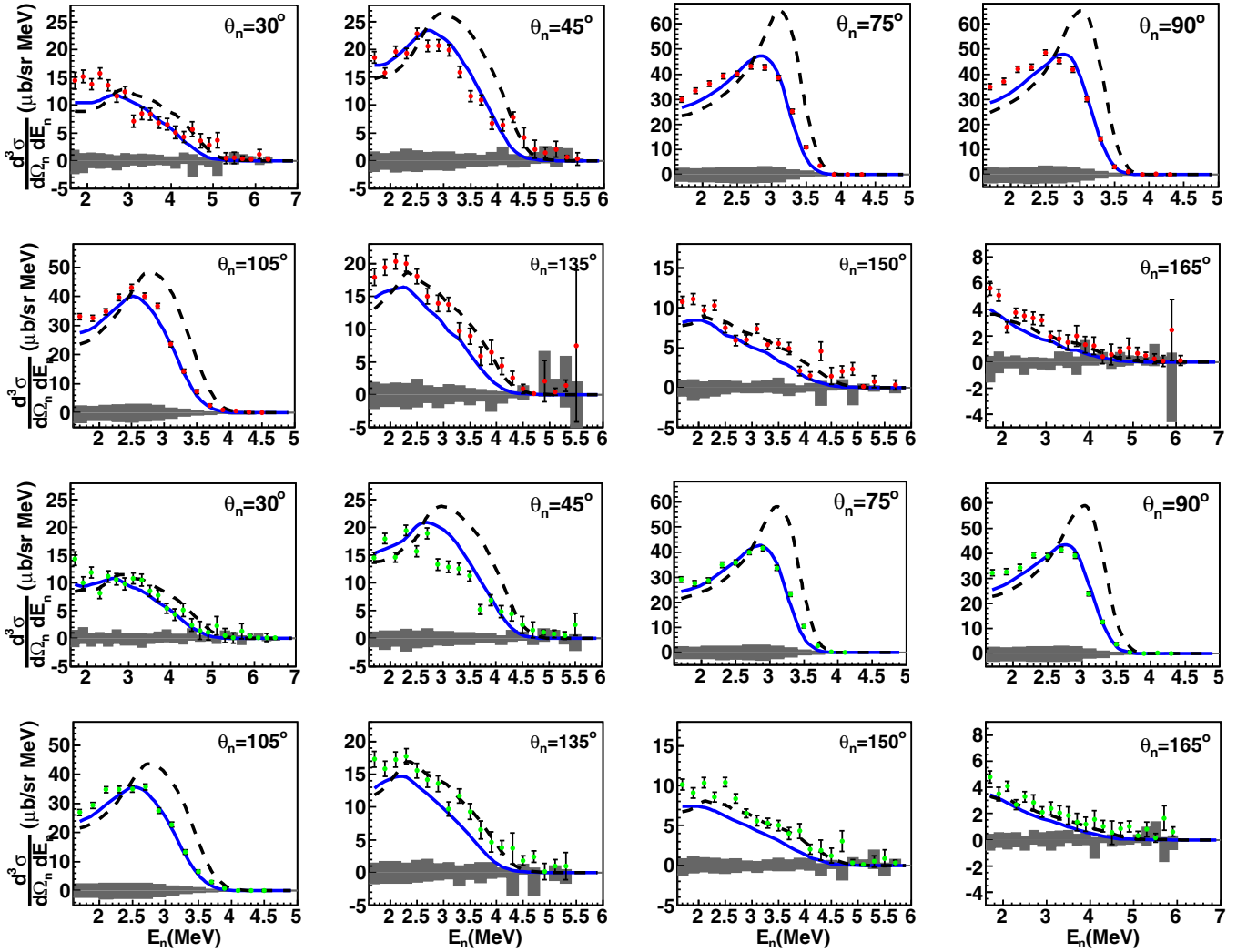
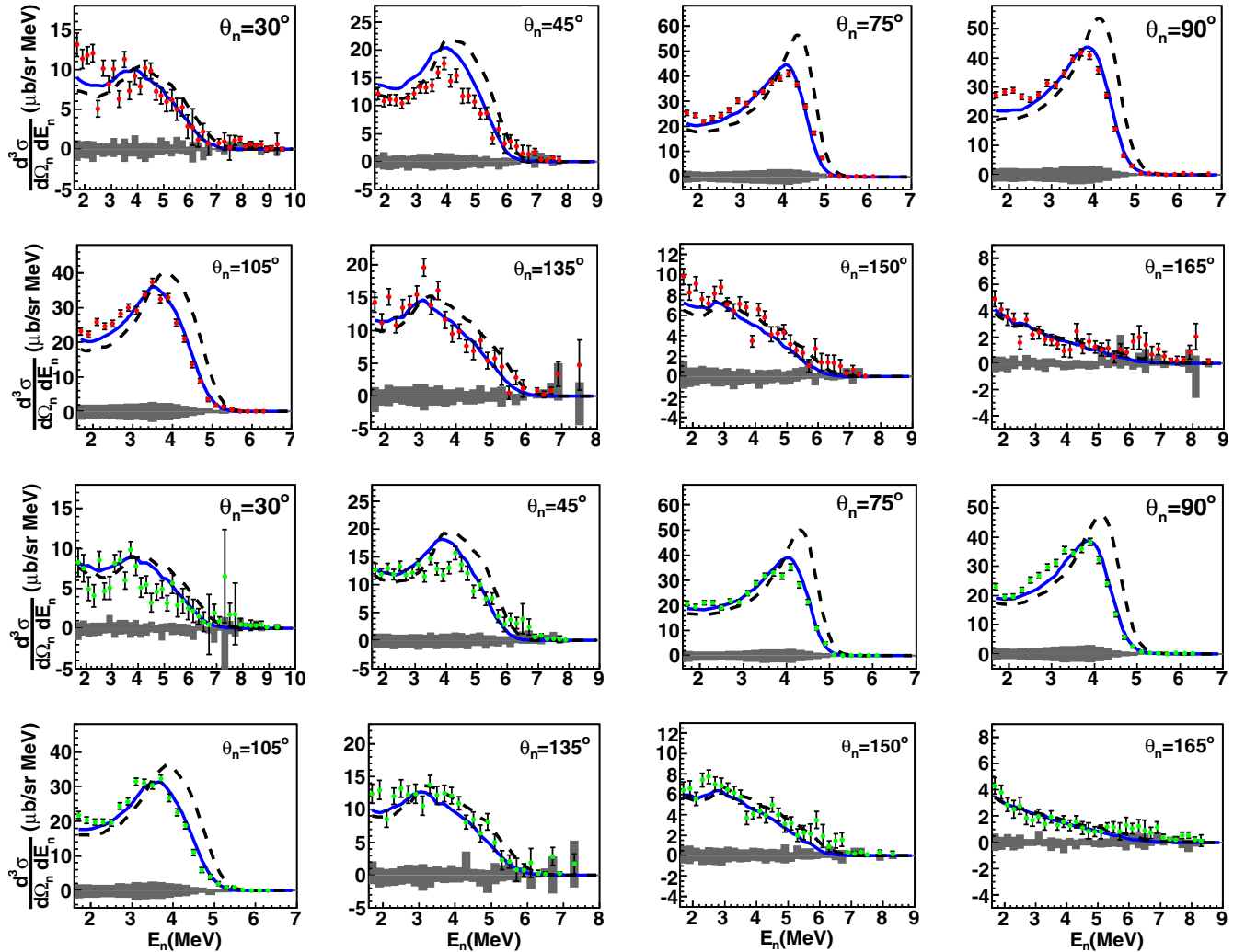


FIG. 4. (Color online) Experimental spin-dependent double-differential cross sections for both parallel (two top rows) and antiparallel (two bottom rows) spin-helicity states as a function of the neutron energy,  $E_n$ , at  $E_\gamma = 12.8$  MeV. They are compared with the calculations of Deltuva *et al.* (solid curve) and Skibiński *et al.* (dashed curve). The neutron energy bin width is 0.2 MeV. The band at the bottom of each histogram shows the combined systematic uncertainties.

of the experiment and the light-output response of the neutron detectors that was determined in Ref. [55].

Two types of systematic uncertainties were identified in this experiment: the bin-dependent uncertainties and the overall normalization uncertainties. The bin-dependent systematic uncertainties were in principle asymmetric and arose from the uncertainty associated with the PH cut location. In order to study the PH cut contribution to the overall systematic uncertainty, the PH cut location was varied and the corresponding double-differential cross sections were extracted. The PH cut location was changed by 0.01 to 0.02 MeV determined by the uncertainty at the cesium edge depending on the detector. The systematic uncertainty due to the PH cut was defined as the difference between the nominal double-differential cross sections and the cross sections obtained after the change of the PH cut location. The contribution of the systematic uncertainty arisen by the PH cut to the overall systematic uncertainty varied from  $\sim 2\%$  to  $\sim 10\%$  depending on the

detector angle with a maximum of  $\sim 20\%$  at  $165^\circ$ . The normalization systematic uncertainties were symmetric and affected only the magnitude of the double-differential cross sections but not the shape of the distributions. The major sources of the normalization uncertainties were  $\varepsilon_i^{\text{sys}}$  (2.8%) [55,56],  $N_t$  (1.3%) in which the main contributor was the uncertainty in the temperature of the  $^3\text{He}$  cell, and  $\Delta\Omega$  (2%), which was determined by the uncertainty of distance from the center of the target to the face of the detectors. The uncertainty of the integrated photon flux (5.7%) was dominated by the uncertainties of  $\text{D}_2\text{O}$  photodisintegration cross sections (4.0% at 12.8 MeV and 4.6% at 14.7 MeV) [49,50], the efficiency of neutron detectors (2.8%), the solid angle (1%), and the thickness of the  $\text{D}_2\text{O}$  target (0.6%). The systematic uncertainty of  $P_{tc}$  was 2.2%. The main contributors to the systematic uncertainty of the target polarization were the uncertainty of the constant  $\kappa$  (1.5%), the number density  $n_{pc}$  (1.1%), and the derivative  $\frac{dV_{EPR}}{dB}$  (0.16%). The photon beam polarization

FIG. 5. (Color online) As in Fig. 4 at  $E_\gamma = 14.7$  MeV.

( $P_b$ ) and its systematic uncertainty were determined by Rusev [57], based on data taken right before our experiment. The beam polarization was found to be consistent with 100% with a systematic uncertainty of 3% for both normal and reversed beam helicity states. Since the beam polarization was not measured during our experiment, we assigned a 5% systematic uncertainty for  $P_b$  to be on the conservative side.

Figures 4 and 5 show the spin-dependent double-differential cross sections obtained at incident photon energies of 12.8 and 14.7 MeV respectively for both spin-helicity states as a function of the outgoing neutron energy and laboratory angles. The solid and dashed curves are the GEANT4 simulation results using the calculations provided by Deltuva *et al.* and Skibiński *et al.* as cross section inputs. The band in each panel shows the overall systematic uncertainties combined in quadrature.

The experimental results are described better by the calculations of Deltuva *et al.* at 45–105° neutron angles. More specifically, the data favor the location of the high-energy neutron peak predicted by Deltuva *et al.* as well as the sharp decrease of the energy distributions predicted by both groups.

At 30°, 135°, 150°, and 165°, the results do not appear to have any discriminating power between the calculations, although the magnitudes and the shapes of the distributions are in general agreement with both calculations. This is due to two reasons: First, the calculations do not differ significantly at the far forward and backward angles and thus the limited statistics do not discriminate between the predictions; second, the finite-geometry effect resulting from the long target is significant and so the reconstructed energies based on the TOF appear to be higher compared to the actual energies predicted by the kinematics. This results in the spread of the neutron counts to a wider energy region and the consequent smearing of the distributions. However, the spin-dependent double-differential cross sections are overall larger in the parallel than those in the antiparallel spin-helicity state as predicted by the calculations for both incident photon energies and all neutron scattering angles.

To correct the observed cross sections for the acceptance effect resulting from the finite length of the  $^3\text{He}$  target and the dimensions of the detector, a further analysis of the data was necessary. First, a conversion of the reconstructed

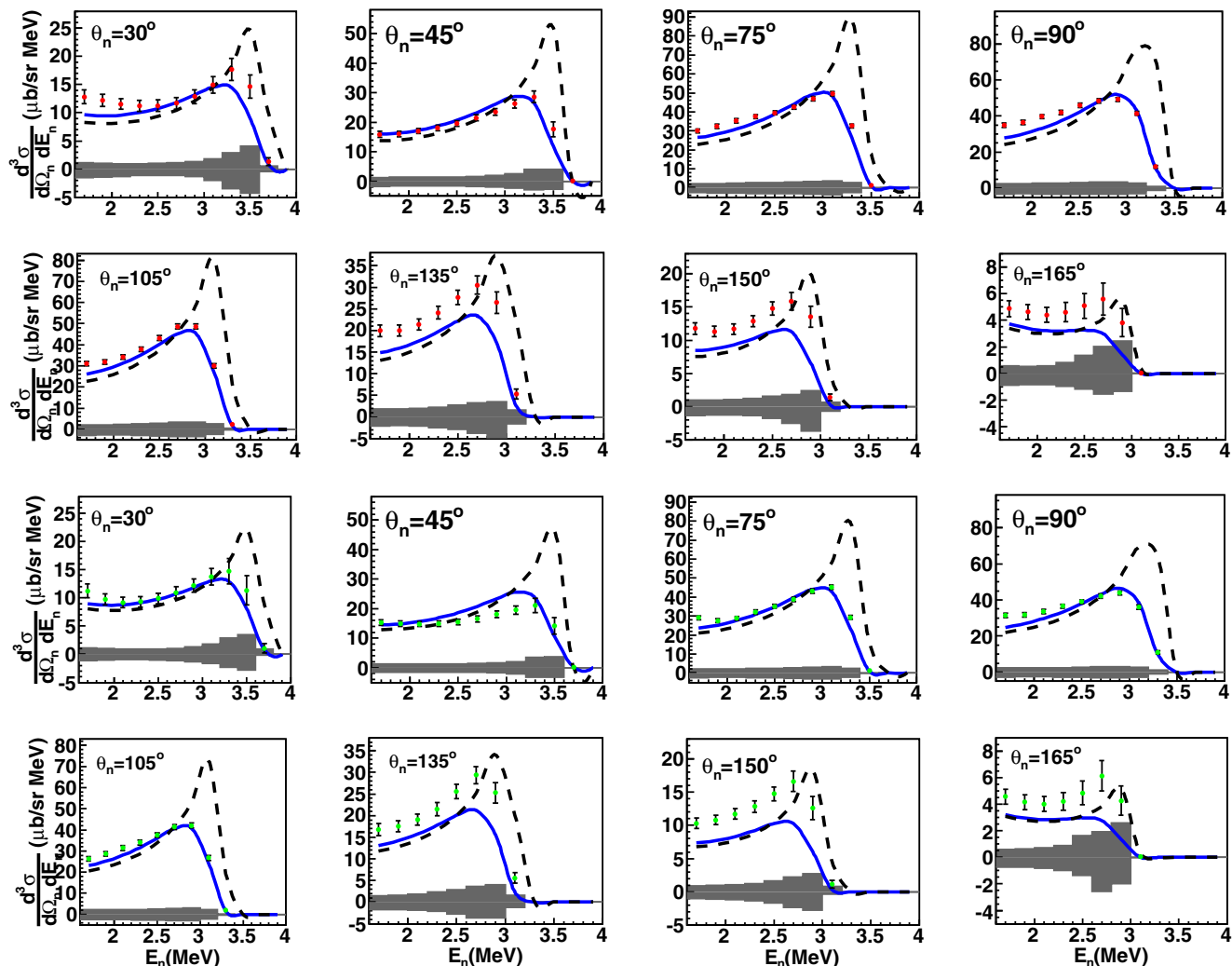


FIG. 6. (Color online) Spin-dependent double-differential cross sections corrected for the acceptance effect, for parallel (two top rows) and antiparallel (two bottom rows) spin-helicity states as a function of the neutron energy,  $E_n$ , compared with the calculations based on Ref. [16] (solid curve) and Ref. [24] (dashed curve) at the incident photon energy of 12.8 MeV. The neutron energy bin width is 0.2 MeV. The band at the bottom of each histogram shows the combined systematic uncertainties.

energies to actual neutron energies took place for all experimental distributions using a two-dimensional map. The two dimensions of the map are the reconstructed energy based on the TOF,  $E_n(\text{TOF})$  and the actual neutron energy,  $E_n$ . Each map element represents the probability of a neutron event with observed  $E_n(\text{TOF})$ , having an actual neutron energy  $E_n$ . The experimental cross section distributions with respect to  $E_n(\text{TOF})$  are multiplied by the map elements bin by bin and the results are projected onto the  $E_n$  axis. The resulting cross sections are further multiplied by the corresponding ratio of the cross sections of Ref. [16] to the GEANT4 simulation results for the extended target using as cross section inputs the calculations provided by the same group. The calculations of Ref. [16] are chosen to perform the acceptance correction since they are in good agreement at all angles and for both incident photon energies with the experimental distributions. Figures 6 and 7 show the spin-dependent double-differential cross sections corrected for the finite geometry effect at

the incident photon energies of 12.8 and 14.7 MeV. While the statistical fluctuations of the distributions with respect to  $E_n(\text{TOF})$  are obvious mainly in the far forward and backward angles due to the spread of the neutron counts to a wider reconstructed energy region, the fluctuations of the distributions with respect to  $E_n$  are smoothed out since the neutrons concentrate in a much smaller actual energy region.

A good agreement between the data and the calculations of Ref. [16] can be seen for all neutron scattering angles, incident photon energies, and both target spin and beam helicity states. Although at the incident photon energy of 12.8 MeV similar agreement is observed for most of the angles, the amplitudes of the experimental distributions appear to be systematically higher than the calculations of Ref. [16] at 135°, 150°, and 165° neutron angles. A good agreement between the double-differential cross sections of the unpolarized three-body breakup of  $^3\text{He}$  and the calculations of Ref. [16] is also reported in Ref. [52]. Apart from the data presented in

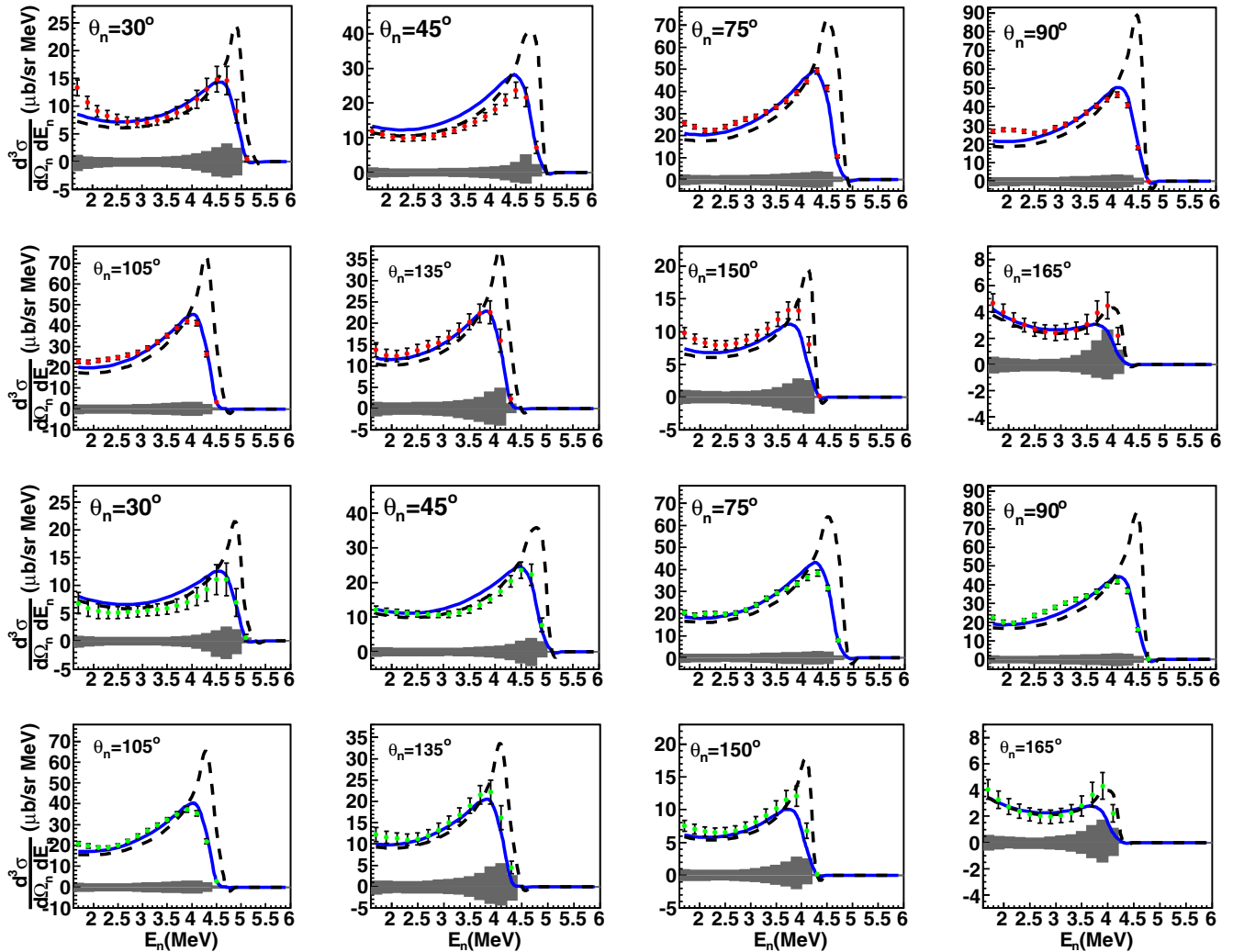


FIG. 7. (Color online) As in Fig. 6 but for the incident photon energy of 14.7 MeV.

Ref. [52], only one other measurement [58] provided data on double-differential cross sections and none of the other measurements prior to our experiment used polarized photon beam and a polarized  $^3\text{He}$  target.

The differences between the two calculations are dominated by the proton-proton Coulomb force that is included only in Ref. [16]. Figure 8 shows a comparison between calculations with various combinations of ingredients for the unpolarized case at the incident photon energy of 14.7 MeV and neutron scattering angle of  $90^\circ$ . Results of Ref. [24] (short-dashed curve) are very similar to the dotted curve, which includes only the CD Bonn  $NN$  potential and the relativistic single-nucleon charge corrections. The magnitude of the distribution changes significantly once the Coulomb force between the protons is taken into account (long-dashed dotted curve). A shift of the high energy peak towards the lower outgoing neutron energies is also observed. The inclusion of  $\Delta$ -isobar (solid curve) only slightly reduces the magnitude of the cross sections.

Although the Coulomb force plays a major role in determining the magnitude of the cross sections, it does not explain the difference observed between the spin-helicity

states. This effect is due to the relativistic single-nucleon charge corrections and the inclusion of  $\Delta$ -isobar as already found in Ref. [16]. Figure 9 shows the double-differential cross section distributions with (solid curve) and without (dashed curve) relativistic single-nucleon charge corrections for each spin-helicity state with all other ingredients being the same. About 2/3 of the overall difference between the spin-helicity states is from the relativistic single-nucleon charge corrections and 1/3 is from the inclusion of the  $\Delta$ -isobar excitation.

The partial single-differential cross sections for  $E_n > 1.5$  MeV were extracted by integrating the corrected double-differential cross section distributions over the outgoing neutron energy. The unmeasured part of the distributions was taken to be equal to the average of the calculated cross sections of Refs. [16,24] for  $E_n$  below 1.5 MeV. For the incident energy of 12.8 MeV (14.7 MeV), the unmeasured part accounted for the 30% (18%) of the total single-differential cross sections at  $75^\circ$ ,  $90^\circ$ , and  $105^\circ$  to 47% (26%) and 66% (50%) for the far backward angles at  $150^\circ$  and  $165^\circ$ , respectively. However, the difference between the calculations was small, as can be seen in Fig. 8, and only varied from 1 to 8% depending on the incident

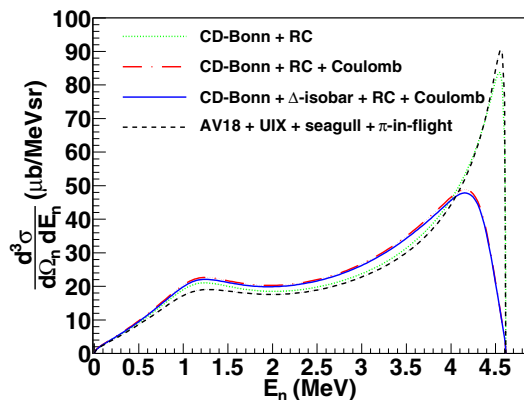


FIG. 8. (Color online) The double-differential cross section as a function of the outgoing neutron energy for the unpolarized three-body photodisintegration of  ${}^3\text{He}$  at  $E_\gamma = 14.7$  MeV and neutron scattering angle of  $90^\circ$ . The short-dashed (black) curve is the calculation from Ref. [24] including AV18 + UIX + seagull + pion-in-flight-terms. The second group of calculations from Ref. [16] are (from top to bottom) dotted (green online) curve, CD Bonn + RC; long-dashed dotted (red online) curve (nearly invisible behind the solid curve), CD Bonn + RC + Coulomb force; and solid (blue online) curve, CD Bonn +  $\Delta$ -isobar + RC + Coulomb force.

photon energy, the spin-helicity state, and the scattering angle. This introduced an additional systematic uncertainty to the single-differential cross sections of no more than 4%.

Figures 10 and 11 show the spin-dependent single-differential cross sections for parallel (filled squares) and antiparallel (open squares) spin-helicity states at  $E_\gamma$  of 12.8 and 14.7 MeV in comparison with both calculations. The cross section data are in general agreement in all angles with the calculations based on Ref. [16]. The results of

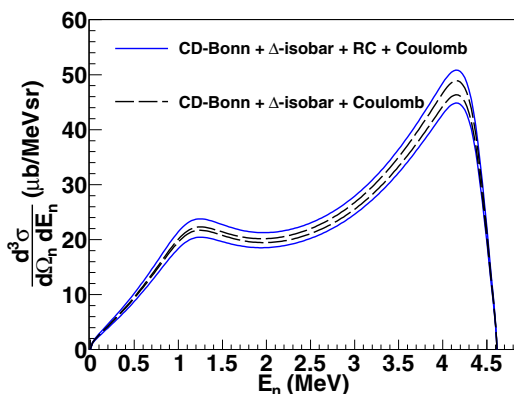


FIG. 9. (Color online) The double-differential cross sections of the three-body photodisintegration of  ${}^3\text{He}$  as a function of the outgoing neutron energy for both parallel (two top curves) and antiparallel (two bottom curves) spin-helicity states at  $E_\gamma = 14.7$  MeV and neutron scattering angle of  $90^\circ$ . The calculations from Ref. [16] are solid (blue online) curves, CD Bonn +  $\Delta$ -isobar + RC + Coulomb; and long-dashed (black) curves, CD Bonn + RC + Coulomb force. The CD Bonn + Coulomb force alone do not have any significant contribution to the difference of the cross sections between the spin-helicity states, and the corresponding curves—if plotted—would be in the middle of the long-dashed curves.

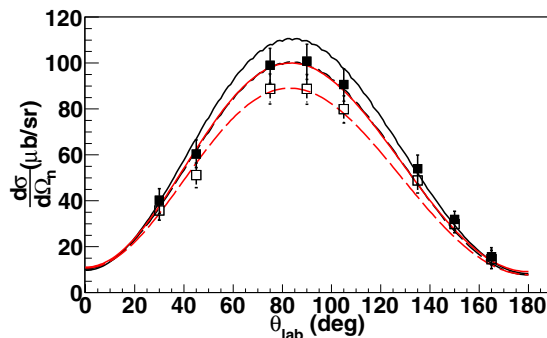


FIG. 10. (Color online) Spin-dependent single-differential cross sections for parallel (filled squares) and antiparallel (open squares) spin-helicity states with statistical and systematic uncertainties as a function of the neutron scattering angle,  $\theta_{\text{lab}}$  at  $E_\gamma = 12.8$  MeV. The data are compared with the calculations based on Ref. [16] (red [gray] curves) and Ref. [24] (black curves). The solid and the long-dashed curves are the calculations for the parallel and antiparallel spin-helicity states, respectively. (The statistical uncertainties in most of the angles are small and cannot be seen in the figure.)

the spin-dependent single-differential cross sections for both incident energies are given in Tables I and II. While the statistical uncertainties vary from less than 1% to  $\sim 3\%$  for both incident photon energies, the systematic uncertainties range from  $\sim 7\%$  to more than  $\sim 20\%$  ( $165^\circ$ ).

Legendre polynomials up to the 4th order were used to fit the differential cross sections acquired for each spin-helicity state at both incident photon energies. The fitted curves were integrated over the angle and the total cross sections were extracted for both energies and the two spin-helicity states. The systematic uncertainties of the total cross sections were determined by varying the differential cross sections from the central values by plus or minus the overall systematic uncertainties that can be seen in Tables I and II and then performing the fit. The systematic uncertainty of the total cross sections was taken as half of the difference between these two integrals of the new fits. The spin-dependent total cross sections and the first data concerning the contributions from the three-body breakup channel to the GDH integrand were presented in Ref. [35]. The extracted spin-dependent cross sections were averaged and the total unpolarized cross sections were calculated for each incident photon energy. Figure 12

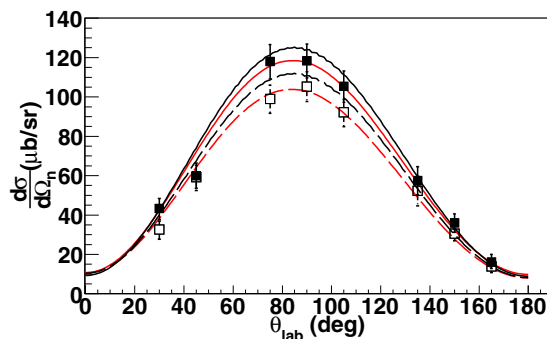


FIG. 11. (Color online) As in Fig. 10 at  $E_\gamma = 14.7$  MeV.

TABLE I. The spin-dependent single-differential cross sections and their statistical and systematic uncertainties, respectively, as a function of the neutron scattering angle at  $E_\gamma = 12.8$  MeV.

Angle	$d\sigma_p/d\Omega(\mu b/sr)$	$d\sigma_A/d\Omega(\mu b/sr)$
30°	$40.2 \pm 1.3 \pm 5.7$	$35.8 \pm 1.5 \pm 4.8$
45°	$60.4 \pm 1.3 \pm 6.2$	$51.2 \pm 1.5 \pm 5.5$
75°	$99.0 \pm 0.9 \pm 7.8$	$88.8 \pm 0.9 \pm 6.7$
90°	$100.8 \pm 1.0 \pm 7.9$	$88.7 \pm 1.0 \pm 6.7$
105°	$90.6 \pm 0.9 \pm 7.3$	$79.9 \pm 0.9 \pm 6.0$
135°	$54.0 \pm 1.4 \pm 6.6$	$48.8 \pm 1.4 \pm 5.6$
150°	$31.9 \pm 1.0 \pm 4.7$	$29.8 \pm 1.0 \pm 3.8$
165°	$15.7 \pm 1.0 \pm 3.9$	$14.5 \pm 1.0 \pm 4.1$

shows the total cross sections from the present experiment together with all data up to 30 MeV. The results are in very good agreement with the most recently published data (filled stars) by an unpolarized  $^3\text{He}$  target at the same incident photon energies [52]. The data were also compared with the total cross section calculations from Ref. [16] (solid curve) and Ref. [24] (dash-dotted curve) and a good agreement was observed again with the results based on the computational approach of Ref. [16].

Although a general agreement between the two models and most of the experimental data can be seen in Fig. 12 for incident photon energy below 15 MeV, a serious discrepancy can be observed above 15 MeV between the data of Refs. [60] (open circles) and [61] (open squares), and the theoretical predictions. This discrepancy leads to the need for more precise data at the energy region above 15 MeV using preferably monochromatic photon energy beams such as the one used at the HI $\gamma$ S facility. However, the performance of similar experiments on the  $^3\text{He}(\vec{\gamma}, n)pp$  reaction at higher energies has to deal with the problem of neutron backgrounds. All glass target cells of polarized  $^3\text{He}$  consist of elements that undergo  $(\gamma, n)$  reactions with cross sections higher or much higher than the cross sections of the reaction of interest. A detailed study of the backgrounds has shown that the same experimental technique described in this paper can be applied to the detection of neutrons up to incident photon energy of 16.5 MeV. Beyond this energy the contribution of oxygen in the air and in the glass to the neutron background becomes important. A possible solution to this background problem would require the detection of one of the protons and the

TABLE II. As in Table I at  $E_\gamma = 14.7$  MeV.

Angle	$d\sigma_p/d\Omega(\mu b/sr)$	$d\sigma_A/d\Omega(\mu b/sr)$
30°	$43.3 \pm 1.5 \pm 5.6$	$32.6 \pm 1.9 \pm 5.0$
45°	$60.0 \pm 1.5 \pm 6.4$	$59.2 \pm 1.5 \pm 6.7$
75°	$118.0 \pm 1.0 \pm 8.8$	$99.1 \pm 1.1 \pm 7.3$
90°	$118.4 \pm 1.1 \pm 8.8$	$105.3 \pm 1.1 \pm 7.7$
105°	$105.4 \pm 1.0 \pm 8.1$	$92.2 \pm 1.0 \pm 7.2$
135°	$57.6 \pm 1.8 \pm 7.4$	$52.3 \pm 1.8 \pm 7.6$
150°	$36.0 \pm 1.0 \pm 4.8$	$30.6 \pm 1.0 \pm 4.3$
165°	$16.0 \pm 0.9 \pm 4.0$	$13.9 \pm 1.0 \pm 3.2$

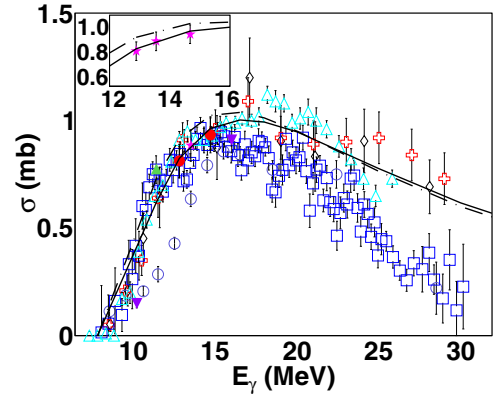


FIG. 12. (Color online) All currently available total cross section data for the  $^3\text{He}(\gamma, n)pp$  reaction up to 30 MeV: Ref. [59] (open diamonds), Ref. [60] (open circles), Ref. [61] (open squares), Ref. [58] (open crosses), Ref. [62] (open upward triangles), Ref. [63] (filled downward triangles), Ref. [52] (filled stars), Ref. [53] (filled upward triangle), and present data (filled circles) in comparison with two calculations based on Ref. [16] (solid curve) and Ref. [24] (dash-dotted curve) theories. In the insert, the data of Ref. [52], which are hidden behind the results of the present work, are shown and compared with the theories. Very good agreement is found between the present results, the data of Ref. [52], and the calculations of Ref. [16].

neutron from the  $^3\text{He}(\gamma, n)pp$  reaction in coincidence. An experiment on  $^3\text{He}(\vec{\gamma}, p)d$  is currently being designed and will use a system of silicon surface barrier detectors for the proton detection, which can be used for the three-body coincidence measurement.

## V. SUMMARY AND CONCLUSIONS

We have carried out the first measurement of the three-body breakup of polarized  $^3\text{He}$  with circularly polarized photons at the incident photon energies of 12.8 and 14.7 MeV. The spin-dependent double- and single-differential cross sections were extracted and compared with the state-of-the-art three-body calculations provided by Deltuva *et al.* and Skibiński *et al.* The experimental results are described better by the calculations based on the computational approach of Ref. [16]. This leads to the conclusion that the inclusion of the proton-proton Coulomb repulsion in the calculations is important for the correct prediction of the magnitude and shape of the cross sections from the  $^3\text{He}(\vec{\gamma}, n)pp$  reaction. The relativistic single-nucleon charge corrections together with the  $\Delta$ -isobar excitation play an important role in the correct estimation of the difference between the spin-helicity-dependent cross sections. Precision experiments and measurements of new observables involving  $3N$  systems will allow for further testing of these calculations.

## ACKNOWLEDGMENTS

The authors thank W. Chen, R. Lu, and X. Zong for their help during the initial stage of this experiment, Michael Souza of Princeton University for making the target cells, Gordon Cates's group from University of Virginia for providing the Rb/K ampules and for sol-gel coating of the target cells, and the

TUNL personnel for the technical support of this experiment. This work is supported by the US Department of Energy under contract numbers DE-FG02-03ER41231, DE-FG02-97ER41033, and DE-FG02-97ER41041; Duke University;

and the Polish National Science Center under Grant No. DEC-2011/01/B/ST2/00578. The numerical calculations of Kraków theoretical group have been performed on the supercomputer clusters of the JSC, Jülich, Germany.

- 
- [1] H. Gao *et al.*, *Phys. Rev. C* **50**, R546 (1994).  
 [2] W. Xu *et al.*, *Phys. Rev. Lett.* **85**, 2900 (2000).  
 [3] M. Meyerhoff *et al.*, *Phys. Lett. B* **327**, 201 (1994).  
 [4] J. Becker *et al.*, *Eur. Phys. J. A* **6**, 329 (1999).  
 [5] D. Rohe *et al.*, *Phys. Rev. Lett.* **83**, 4257 (1999).  
 [6] J. Bermuth *et al.*, *Phys. Lett. B* **564**, 199 (2003).  
 [7] S. Riordan *et al.*, *Phys. Rev. Lett.* **105**, 262302 (2010).  
 [8] P. L. Anthony *et al.*, *Phys. Rev. D* **54**, 6620 (1996).  
 [9] K. Abe *et al.*, *Phys. Rev. Lett.* **79**, 26 (1997).  
 [10] K. Ackerstaff *et al.*, *Phys. Lett. B* **404**, 383 (1997).  
 [11] M. Amarian *et al.*, *Phys. Rev. Lett.* **89**, 242301 (2002).  
 [12] X. Qian *et al.*, *Phys. Rev. Lett.* **107**, 072003 (2011).  
 [13] P.-H. Chu *et al.*, *Phys. Rev. D* **87**, 011105(R) (2013).  
 [14] L. D. Faddeev, *Zh. Eksp. Teor. Fiz.* **39**, 1459 (1960) [*Sov. Phys. JETP* **12**, 1041 (1961)].  
 [15] E. O. Alt, P. Grassberger, and W. Sandhas, *Nucl. Phys. B* **2**, 167 (1967).  
 [16] A. Deltuva, L. P. Yuan, J. Adam, A. C. Fonseca, and P. U. Sauer, *Phys. Rev. C* **69**, 034004 (2004); A. Deltuva, A. C. Fonseca, and P. U. Sauer, *ibid.* **71**, 054005 (2005); **72**, 054004 (2005); **80**, 064004 (2009).  
 [17] V. G. J. Stoks, R. A. M. Klomp, C. P. F. Terheggen, and J. J. de Swart, *Phys. Rev. C* **49**, 2950 (1994).  
 [18] R. B. Wiringa, V. G. J. Stoks, and R. Schiavilla, *Phys. Rev. C* **51**, 38 (1995).  
 [19] R. Machleidt, F. Sammarruca, and Y. Song, *Phys. Rev. C* **53**, R1483 (1996).  
 [20] A. Deltuva, R. Machleidt, and P. U. Sauer, *Phys. Rev. C* **68**, 024005 (2003).  
 [21] A. Deltuva, A. C. Fonseca, and P. U. Sauer, *Ann. Rev. Nucl. Part. Sci.* **58**, 27 (2008).  
 [22] J. Golak, R. Skibiński, W. Glöckle, H. Witała, A. Nogga, and H. Kamada, *Phys. Rep.* **415**, 89 (2005), and references therein.  
 [23] J. Carlson, V. R. Pandharipande, and R. B. Wiringa, *Nucl. Phys. A* **401**, 59 (1983).  
 [24] R. Skibiński, J. Golak, H. Kamada, H. Witała, W. Glöckle, and A. Nogga, *Phys. Rev. C* **67**, 054001 (2003); R. Skibiński, J. Golak, H. Witała, W. Glöckle, A. Nogga, and H. Kamada, *ibid.* **72**, 044002 (2005).  
 [25] D. Rospędzik, J. Golak, S. Kölling, E. Epelbaum, R. Skibiński, H. Witała, and H. Krebs, *Phys. Rev. C* **83**, 064004 (2011).  
 [26] S. Weinberg, *Phys. Lett. B* **295**, 114 (1992).  
 [27] S. Kölling, E. Epelbaum, H. Krebs, and U.-G. Meißner, *Phys. Rev. C* **80**, 045502 (2009).  
 [28] S. D. Drell and A. Hearn, *Phys. Rev. Lett.* **16**, 908 (1966); S. B. Gerasimov, *Yad. Fiz.* **2**, 598 (1965) [*Sov. J. Nucl. Phys.* **1**, 430 (1966)].  
 [29] H. Dutz *et al.*, *Phys. Rev. Lett.* **93**, 032003 (2004), and references therein.  
 [30] H. Dutz *et al.*, *Phys. Rev. Lett.* **94**, 162001 (2005), and references therein.  
 [31] J. Ahrens *et al.*, *Phys. Lett. B* **672**, 328 (2009), and references therein.  
 [32] M. W. Ahmed, M. A. Blackston, B. A. Perdue, W. Tornow, H. R. Weller, B. Norum, B. Sawatzky, R. M. Prior, and M. C. Spraker, *Phys. Rev. C* **77**, 044005 (2008).  
 [33] H. Gao, W. Chen, and X. Zong, *Proc. Sci.* **CD09**, 101 (2009).  
 [34] P. Aguar Bartolomé *et al.*, *Phys. Lett. B* **723**, 71 (2013).  
 [35] G. Laskaris *et al.*, *Phys. Rev. Lett.* **110**, 202501 (2013).  
 [36] H. R. Weller, M. W. Ahmed, H. Gao, W. Tornow, Y. K. Wu, M. Gai, and R. Miskimen, *Prog. Part. Nucl. Phys.* **62**, 257 (2009).  
 [37] W. Happer, *Rev. Mod. Phys.* **44**, 169 (1972).  
 [38] W. Lorenzon, T. R. Gentile, H. Gao, and R. D. McKeown, *Phys. Rev. A* **47**, 468 (1993).  
 [39] M. V. Romalis and G. D. Cates, *Phys. Rev. A* **58**, 3004 (1998), and references therein.  
 [40] K. Kramer, X. Zong, R. Lu, D. Dutta, H. Gao, X. Qian, Q. Ye, X. Zhu, T. Averett, and S. Fuchs, *Nucl. Instrum. Methods Phys. Res., Sect. A* **582**, 318 (2007).  
 [41] W. Korsch, TJNAF E94-010 Technical Note E94010-TN-11 (unpublished).  
 [42] Q. Ye, G. Laskaris, W. Chen, H. Gao, W. Zheng, X. Zong, T. Averett, G. D. Cates, and W. A. Tobias, *Eur. Phys. J. A* **44**, 55 (2010).  
 [43] D. R. Lide, *Handbook of Chemistry and Physics*, 85th ed. (CRC Press, Boca Raton, FL, 2004).  
 [44] A. Lepretre, H. Beil, R. Bergère, P. Carlos, and A. Veysié, *Nucl. Phys. A* **175**, 609 (1971).  
 [45] V. A. Zheltonozhsky, V. M. Mazur, Z. M. Bigan, and D. M. Symochko, *Yad. Fiz. Energ.* **2**, 13 (2008).  
 [46] A. Veysié, H. Beil, R. Bergère, P. Carlos, A. Lepretre, and A. De Miniac, *Nucl. Phys. A* **227**, 513 (1974).  
 [47] D. V. Webb, E. G. Muirhead, and B. M. Spicer, *Nucl. Phys. A* **171**, 324 (1971).  
 [48] G. F. Knoll, *Radiation Detection and Measurement*, 4th ed. (John Wiley & Sons, Hoboken, NJ, 2010).  
 [49] R. Bernabei *et al.*, *Phys. Rev. Lett.* **57**, 1542 (1986).  
 [50] Y. Birenbaum, S. Kahane, and R. Moreh, *Phys. Rev. C* **32**, 1825 (1985).  
 [51] M. A. Blackston, Ph.D. thesis, Duke University, 2007 (unpublished).  
 [52] B. A. Perdue, Ph.D. thesis, Duke University, 2010 (unpublished); B. A. Perdue, M. W. Ahmed, S. S. Henshaw, P.-N. Seo, S. Stave, H. R. Weller, P. P. Martel, and A. Teymurazyan, *Phys. Rev. C* **83**, 034003 (2011).  
 [53] X. Zong, Ph.D. thesis, Duke University, 2010 (unpublished).  
 [54] Mesytec GmbH & Co. KG, *Four Channel Particle Discriminator Module for Liquid Scintillators*, <http://www.mesytec.com/datasheets/MPD-4.pdf>  
 [55] D. E. González Trotter, F. Salinas Meneses, W. Tornow, A. S. Crowell, C. R. Howell, D. Schmidt, and R. L. Walter, *Nucl. Instr. Meth. A* **599**, 234 (2009).

- [56] H. R. Setze *et al.*, *Phys. Lett. B* **388**, 229 (1996).
- [57] G. Rusev *et al.* (private communication).
- [58] A. N. Gorbunov, in *Photonuclear and Photomesic Processes*, edited by D. V. Skobel'tsyn (Consultants Bureau, New York, 1974), Vol. 71, pp. 1–117.
- [59] A. N. Gorbunov and A. T. Varfolomeev, *Phys. Lett.* **11**, 137 (1964).
- [60] H. M. Gerstenberg and J. S. O'Connell, *Phys. Rev.* **144**, 834 (1966).
- [61] B. L. Berman, S. C. Fultz, and P. F. Yergl, *Phys. Rev. C* **10**, 2221 (1974).
- [62] D. D. Faul, B. L. Berman, P. Meyer, and D. L. Olson, *Phys. Rev. C* **24**, 849 (1981).
- [63] S. Naito *et al.*, *Phys. Rev. C* **73**, 034003 (2006).